nature structural & molecular biology

ARTICLES

https://doi.org/10.1038/s41594-018-0117-6

Structure of the mechanosensitive OSCA channels

Mingfeng Zhang[1,2,3], Dali Wang[4], Yunlu Kang[1], Jing-Xiang Wu[1,2], Fuqiang Yao[5], Chengfang Pan[5], Zhiqiang Yan[5*], Chen Song[2,3,4*] and Lei Chen[1,2*]

Mechanosensitive ion channels convert mechanical stimuli into a flow of ions. These channels are widely distributed from bacteria to higher plants and humans, and are involved in many crucial physiological processes. Here we show that two members of the OSCA protein family in *Arabidopsis thaliana*, namely *At*OSCA1.1 and *At*OSCA3.1, belong to a new class of mechanosensitive ion channels. We solve the structure of the *At*OSCA1.1 channel at 3.5-Å resolution and *At*OSCA3.1 at 4.8-Å resolution by cryo-electron microscopy. OSCA channels are symmetric dimers that are mediated by cytosolic inter-subunit interactions. Strikingly, they have structural similarity to the mammalian TMEM16 family proteins. Our structural analysis accompanied with electrophysiological studies identifies the ion permeation pathway within each subunit and suggests a conformational change model for activation.

Mechanical stimuli represent important environmental cues that living organisms have to sense and cope with. One class of mechanosensors are mechanosensitive channels, which gate the ion flow on mechanical stimuli. These channels are present in nearly all of the kingdoms of living organisms. Among them, the MscS and MscL families are found in bacteria and involved in the osmolality shock response[1]; NOMPC are found in insects and involved in touch and hearing[2–5]; the K2P family potassium channel TRAAK are found in animals and humans and are involved in mechanical nociception[6]; and recently identified Piezo channels in animals are implicated in sensing of light touch, vascular blood flow, and proprioception[7]. There are also mechanosensitive ion channels identified in plants, such as the MSL, TPK, and MCA channels[8]. On the basis of their activation mechanisms, mechanosensitive channels can be divided into two distinct classes. One class of mechanosensitive channels, such as NOMPC, relies on the cytoskeleton for mechanosensitivity. The ankyrin repeat domain of NOMPC[9] forms 'helical springs' that interact with microtubules, and disruption of microtubules diminishes the mechanosensitive currents of NOMPC[10]. In contrast, the other classes of mechanosensitive channels directly sense the 'force from lipid' and do not depend on the cytoskeleton for mechanosensitivity[11,12]. These channels include MscL[13–15], the TRAAK channel[16,17], the TREK1 channel[17], and Piezo1[18,19]. Some mechanosensitive ion channels, such as MscS and MscL in bacteria, can be activated by force from lipid as a consequence of osmolality changes[1]. In plants, hyperosmotic stress is an environmental cue for drought, and plants respond to high osmolality via a range of physiological processes, including the rapid closure of stomatal apertures[20]. One key molecule that serves as an osmosensor in plants was recently identified to be an ion channel, namely *At*OSCA1.1 (*Arabidopsis thaliana* reduced hyperosmolality induced $[Ca^{2+}]_i$ increase 1, OSCA1)[21]. Similarly to their plant counterparts, *Sc*CSC1 from yeast and *Hs*CSC1 from humans also form calcium-permeable ion channels that are activated by high osmotic shock[22], suggesting that the OSCA ion channel family has conserved osmosensing functions from yeast to humans. However, the working mechanisms of the OSCA channel are unknown owing to a lack of structural information. In this study, we show that *At*OSCA1.1 and its paralog *At*OSCA3.1 (also named early responsive to dehydration stress 4, ERD4) are mechanosensitive channels. We solve the de novo structures of the *At*OSCA1.1 and *At*OSCA3.1 channels by cryo-EM. The structures reveal the architecture of this evolutionarily conserved OSCA channel family. Along with electrophysiological experiments, we also find the pore location and propose an activation mechanism of OSCA channels.

Results

***At*OSCA1.1 and *At*OSCA3.1 are mechanosensitive channels.** We introduced a C-terminal green fluorescent protein (GFP) tag to track protein expression. As previously reported, Free Style 293-F cells transfected with C-terminally GFP-tagged *At*OSCA1.1 indicated a hyperosmolality-induced Ca^{2+} increase (Supplementary Fig. 1a)[21]. As some osmosensing channels such as MscS and MscL can be activated by mechanical force, we sought to test whether the *At*OSCA1.1 channel is also mechanosensitive. We found that the *At*OSCA1.1 channel could be reproducibly activated by applying pressure inside the patch pipette in inside-out mode (Fig. 1a,b). In contrast, overexpression of GFP alone by transfection did not generate any detectable mechanosensitive currents within the pressure range tested (Fig. 1a,b). The half-activation pressure of *At*OSCA1.1 was around −99 mm Hg (Fig. 1c), which is lower than that of *Hs*TRAAK measured using patch pipettes with similar geometry (Supplementary Fig. 1b). Furthermore, we used the high-affinity microtubule polymerization inhibitor nocodazole[23] to evaluate whether the mechanosensitivity of *At*OSCA1.1 requires microtubule dynamics. Addition of 100 nM nocodazole to an inside-out patch (for 3–7 min) only slightly reduced mechanosensitive currents, suggesting that microtubule dynamics is not necessary for mechanosensitivity in *At*OSCA1.1 (Fig. 1d). Moreover, we found that incubation of the recording patch with conical lipid lysophosphatyidylcholine (LPC) enhanced channel activity (Fig. 1e,f), similarly to the MscL channel that senses force from lipid[14].

[1]State Key Laboratory of Membrane Biology, Institute of Molecular Medicine, Peking University, Beijing Key Laboratory of Cardiometabolic Molecular Medicine, Beijing, China. [2]Peking-Tsinghua Center for Life Sciences, Peking University, Beijing, China. [3]Academy for Advanced Interdisciplinary Studies, Peking University, Beijing, China. [4]Center for Quantitative Biology, Academy for Advanced Interdisciplinary Studies, Peking University, Beijing, China. [5]State Key Laboratory of Medical Neurobiology, Human Phenome Institute, Ministry of Education Key Laboratory of Contemporary Anthropology, Collaborative Innovation Center of Genetics and Development, Department of Physiology and Biophysics, School of Life Sciences, Fudan University, Shanghai, China. *e-mail: zqyan@fudan.edu.cn; c.song@pku.edu.cn; chenlei2016@pku.edu.cn

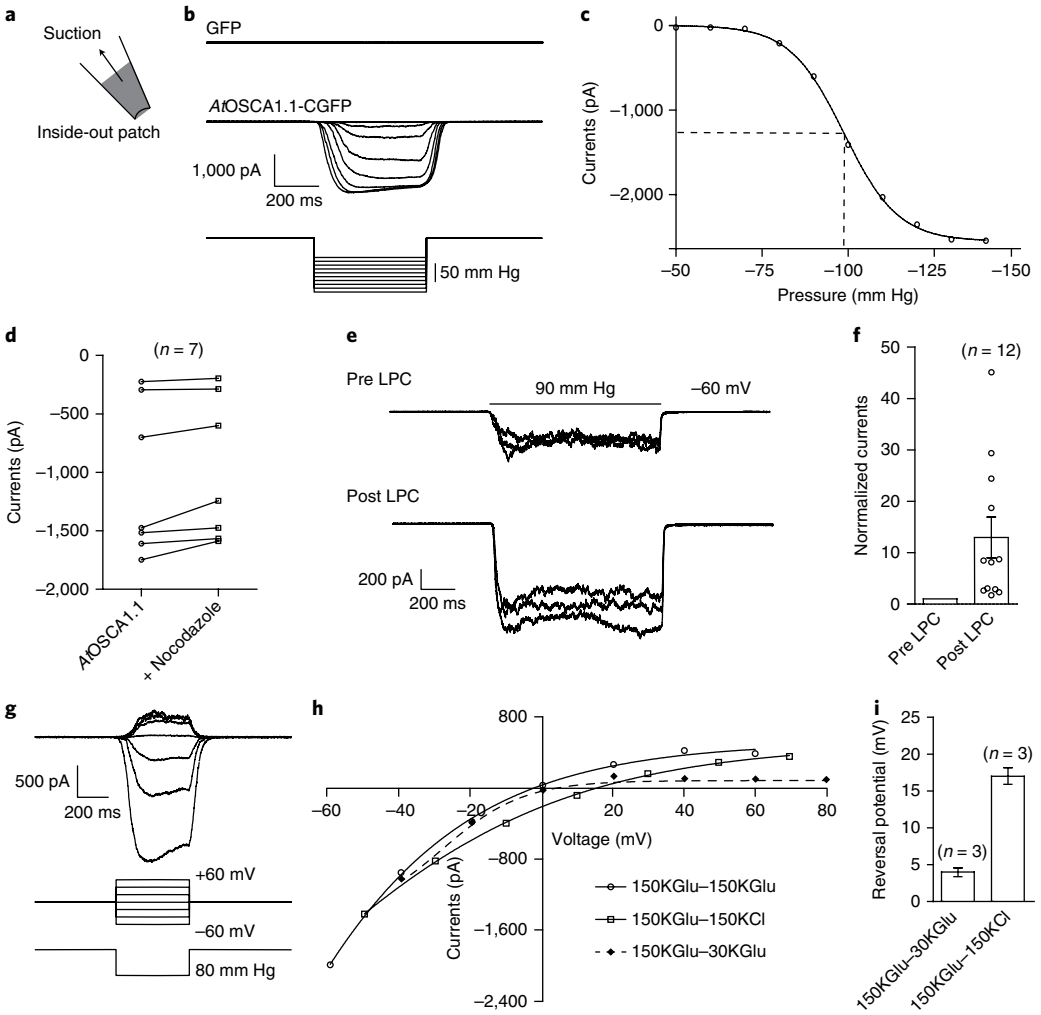

Fig. 1 | *At*OSCA1.1 is a mechanosensitive channel. a, Cartoon representation of the pressure clamp setup in an inside-out mode. Negative pressure was applied inside the patch pipette. **b**, Representative traces of negative-pressure-activated currents recorded from cells transfected with GFP and *At*OSCA1.1-CGFP at a holding potential of −60 mV. Negative pressure was applied from −50 to −140 mm Hg with 10 mm Hg per step. Experiments were repeated 14 times and similar results were obtained. **c**, Currents from **b** were fitted with the Boltzmann equation (P_{50} = −98.83 ± 0.89 mm Hg). **d**, Currents before and after 100 nM nocodazole treatment of the same patch. Currents were recorded at a holding potential of −60 mV and were evoked by pressure of −80 mm Hg (n = 7 independent experiments). **e**, Representative traces of negative-pressure-activated *At*OSCA1.1 currents before and after 3 μM lysophosphatidylcholine (LPC) treatment of the same patch. Currents were recorded at a holding potential of −60 mV and were evoked by three repeated pressure applications of −80 mm Hg. **f**, Currents after 3 μM LPC treatment of the same patch were normalized to the currents before LPC treatment (n = 12 independent experiments, data are mean ± s.e.m.). **g**, Representative traces of negative-pressure-activated *At*OSCA1.1 currents at a holding potential from −60 mV to 60 mV with 20 mV per step evoked by the pressure of −80 mm Hg. Both pipette and bath solutions were 10 mM HEPES (pH 7.2) and 150 mM potassium gluconate (KGlu). Experiments were repeated three times and similar results were obtained. **h**, Representative *I*–*V* curves of the *At*OSCA1.1 channel. Currents were elicited by the same pressure. The pipette solutions were the same as in **g**, while the bath solutions were as follows: 10 mM HEPES (pH 7.2) and 150 mM KGlu (150KGlu–150KGlu, solid line with hollow circles); 10 mM HEPES (pH 7.2), 30 mM KGlu, and 240 mM sucrose (150KGlu–30KGlu, dashed line with solid diamonds); and 10 mM HEPES (pH 7.2) and 150 mM KCl (150KGlu–150KCl, solid line with hollow squares). **i**, The reversal potential of the *At*OSCA1.1 channel in the indicated solutions (n = 3 independent experiments, data are mean ± s.e.m.).

We analyzed the ion selectivity of the *At*OSCA1.1 channel and found that currents are modulated by voltage and the relative permeabilities $P_K/P_{Glu} \approx 0.7–0.8$ and $P_{Cl}/P_{Glu} \approx 0.11–0.15$ (Fig. 1g–i). In addition, we characterized *At*OSCA3.1 (ERD4), another OSCA family members in plants[24], and found that *At*OSCA3.1 also constitutes a mechanosensitive ion channel that responds to very high negative pressure ($P_{50} > 200$ mm Hg) (Supplementary Fig. 2a,b). *At*OSAC3.1 has an ion selectivity of $P_K/P_{Glu} \approx 0.9–1.0$, but the chloride permeability is very low (Supplementary Fig. 2c,d). Structural studies were further employed to uncover the structure and mechanism of these newly identified mechanosensitive ion channels.

Architecture of the OSCA channel. The heterologously expressed *At*OSCA1.1 channel protein was sufficiently stable when extracted in detergent micelles (Supplementary Fig. 1d–h). Each *At*OSCA1.1 polypeptide chain is composed of 772 amino acids. On fluorescence-detection size-exclusion chromatography (FSEC)[25], the C-terminally GFP-tagged *At*OSCA1.1 migrated slightly slower than the C-terminally GFP-tagged mouse two-pore channel 1 (*m*TPC1) (Supplementary Fig. 1d). TPC1 is a well-characterized dimeric ion channel with 817 amino acids in each protomer[26,27]. This suggests that *At*OSCA1.1 might also be a dimer. The purified *At*OSCA1.1 protein migrated as smeared bands on SDS–PAGE (Supplementary Fig. 1e,f). PNGase F treatment sharpened

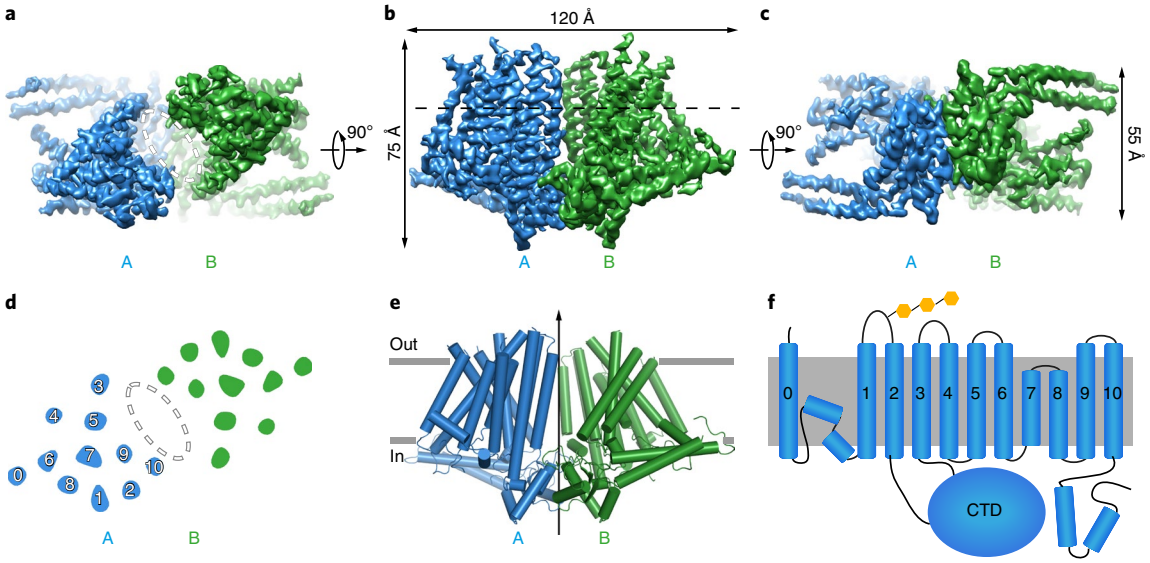

Fig. 2 | Overall structure of the *At*OSCA1.1 channel. a–c, Cryo-EM density maps showing the top view (**a**), side view (**b**), and bottom view (**c**) of the *At*OSCA1.1 channel. Each subunit of the dimer is shown in blue (molecule A) or green (molecule B). A large cavity between the two transmembrane domains is marked by the elliptical dashed line. **d**, Top view of the cross-section of the transmembrane layer at the position indicated by the dashed line in **b**. Transmembrane helices of each subunit are colored the same as in **a**. The 11 transmembrane helices of each subunit are marked by 0–10. **e**, Cartoon representation of *At*OSCA1.1 from a side view. Helices are shown as cylinders. The approximate extent of the phospholipid bilayer is shown as thick gray lines. The arrow denotes the dyad axis within the dimers. **f**, Topology of a single *At*OSCA1.1 subunit. The 11 transmembrane helices are marked by 0–10. The cytoplasmic domain between M2 and M3 is marked as CTD. The phospholipid bilayer is shown as gray layers. The N-linked glycosylation of N138 on the M1–M2 loop is shown in orange.

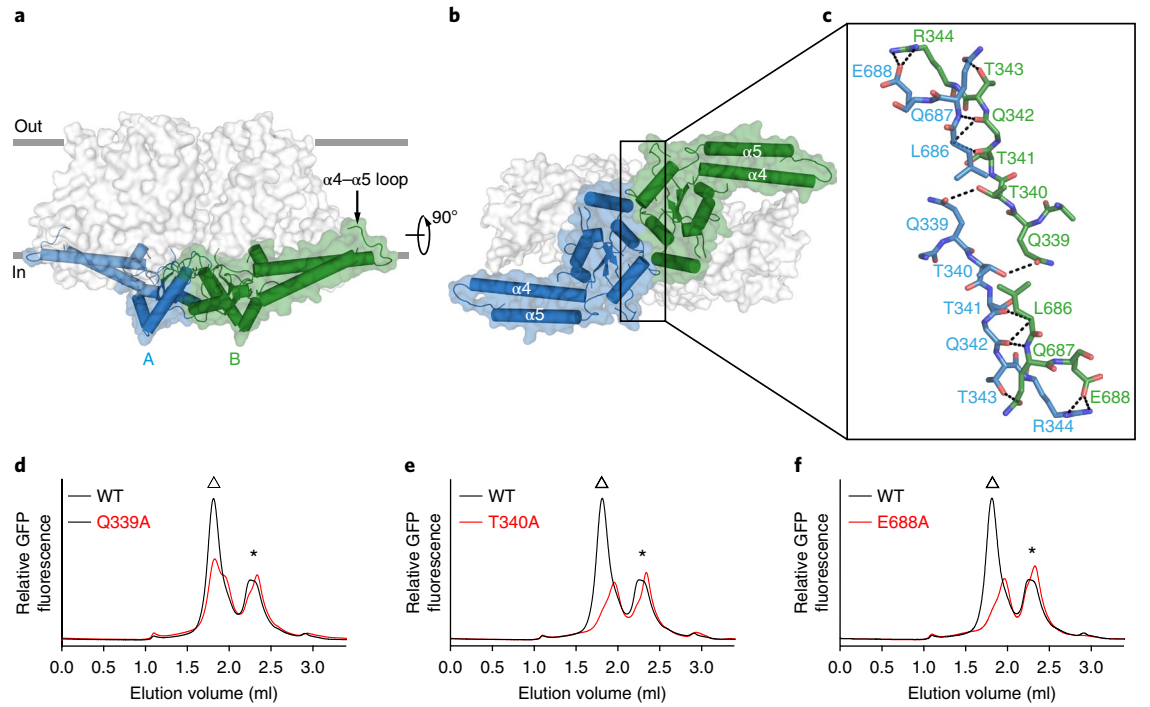

Fig. 3 | Cytoplasmic dimer interface of the *At*OSCA1.1 channel. a, Surface representation of *At*OSCA1.1 from a side view. Transmembrane domains are in gray and cytoplasmic domains are colored the same as in Fig. 2. **b**, Bottom view of *At*OSCA1.1. The dimer interface is marked by a rectangular box. **c**, Close-up view of the dimer interface boxed in **b**. Hydrogen bonds and electrostatic interactions are shown by dashed lines. **d–f**, Representative FSEC traces of the Q339A (**d**), T340A (**e**), and E688A (**f**) mutants (red) are compared to that of wild-type (WT) *At*OSCA1.1 (black). The position of the *At*OSCA1.1 dimer peak is denoted by the triangles above. Asterisks denote the position of free GFP.

the smeared bands into a single band and shifted the FSEC peak position to a lower molecular weight (Supplementary Fig. 1g,h). This indicates that *At*OSCA1.1 is N-linked glycosylated when heterologously expressed in mammalian cells. Indeed, introduction of an N138Q mutation in Nx(T/S), the consensus motif for N-linked glycosylation, greatly reduced the sugar decoration as

Table 1 | Cryo-EM data collection, refinement, and validation statistics

	*At*OSCA1.1(EMDB-6822)(PDB 5YD1)	*At*OSCA3.1(EMDB-6875)(PDB 5Z1F)
Data collection and processing		
Magnification	50,000×	47,400×
Voltage (kV)	300	300
Electron exposure (e^{-} Å^{-2})	50	52
Defocus range (μm)	−1.5 to −3.5	−1.5 to −3.5
Pixel size (Å)	1	1.055
Symmetry imposed	*C2*	*C2*
Initial particle images (no.)	415,262	49,787
Final particle images (no.)	115,697	16,322
Map resolution (Å)	3.52	4.80
FSC threshold	0.143	0.143
Map resolution range (Å)	128–3.52	128–4.80
Refinement		
Initial model used	De novo building	5YD1
Model resolution (Å)	3.52	4.80
FSC threshold	0.143	0.143
Model resolution range (Å)	128–3.52	28–4.80
Map sharpening *B* factor (Å^2)	−159.0	−272.4
Model composition		
Non-hydrogen atoms	9,398	8,480
Protein residues	9,398	8,480
Ligands	0	0
B factors (Å^2)		
Protein	125.91	92.11
R.m.s. deviations		
Bond lengths (Å)	0.006	0.005
Bond angles (°)	1.110	0.866
Validation		
MolProbity score	2.81	3.00
Clash score	21.01	25.18
Poor rotamers (%)	6.41	5.04
Ramachandran plot		
Favored (%)	94.39	89.17
Allowed (%)	5.27	9.81
Disallowed (%)	0.34	1.02

observed from a shift to the right in FSEC peak position and insensitivity to PNGase F treatment (Supplementary Fig. 1g,h). However, the N124Q mutation had little effect on the N-linked glycosylation states (Supplementary Fig. 1g,h). These results suggest that N138 is one of the major N-linked glycosylation sites of *At*OSCA1.1 and is located extracellularly. This corroborates the topology of our structural model in which N138 occurs on an extracellular loop between M1 and M2 (Fig. 2).

The purified *At*OSCA1.1 protein was subjected to cryo-EM single-particle analysis (Supplementary Fig. 3a). The 2D class averages suggested that the protein is a dimer with twofold rotational symmetry (Supplementary Fig. 3b). Subsequent 3D reconstruction, classification, and refinement yielded a map with an average resolution of 3.5 Å (Supplementary Fig. 3c–e and Table 1). The central part of the channel has better local resolution than the average, while the flexible peripheral parts of the molecule and detergent micelle shell have the lowest local resolution (Supplementary Fig. 4a,b). The map was of sufficient quality to enable us to trace the Cα atoms for the stable parts of the molecule, and the bulky side chains allowed us to assign the sequence of the model (Supplementary Fig. 4c–e). Furthermore, we purified and solved the cryo-EM structure of *At*OSCA3.1 at 4.8-Å resolution (Supplementary Figs. 2e,f and 5, and Table 1). The overall architecture and conformation of *At*OSCA3.1 is largely the same as that of *At*OSCA1.1 (Supplementary Fig. 5), further emphasizing the structural conservation of this protein family.

*At*OSCA1.1 is a symmetric dimer with a twofold rotation axis perpendicular to the membrane bilayer. The channel has a two-layer architecture: the upper transmembrane domain and lower cytosolic domain, occupying 3D space with a size of 120 Å × 55 Å × 75 Å (Fig. 2a–c). The topology of the 11 transmembrane helices (M0 to M10) can be unambiguously determined, and contains an extracellular N terminus and cytosolic C terminus (Fig. 2d–f). A huge cavity that is filled with disordered detergents/phospholipids insulates the two individual transmembrane domains, while the cytosolic domains bridge two subunits to form a dimer (Fig. 2d,e).

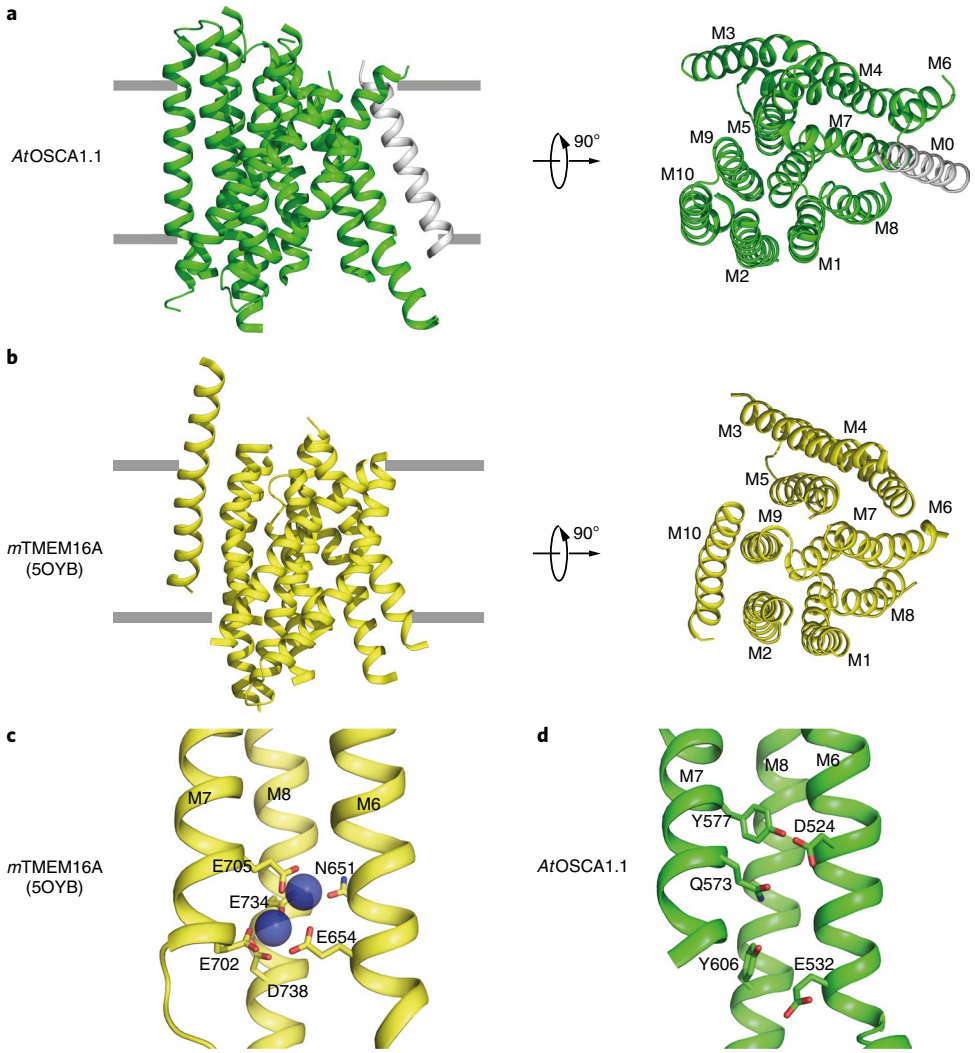

Fig. 4 | Structural comparison of *At*OSCA1.1 and *m*TMEM16A. a,**b**, Side view (left) and bottom view (right) of the transmembrane domains of *At*OSCA1.1 (**a**) and *m*TMEM16A (PDB 5OYB) (**b**) shown in green and yellow. M0 of *At*OSCA1.1 is shown in gray. **c**, Calcium-binding sites of *m*TMEM16A. Calcium ions are shown as blue spheres. **d**, The corresponding region of *At*OSCA1.1.

Cytoplasmic dimer interface of the OSCA channels. The cytosolic domain is mainly folded by the intracellular M2–M3 loop and C terminus. It has an elongated two-blade propeller shape and caps below the transmembrane domain. Each blade is formed by two antiparallel α helices, α4 and α5, which protrude from the center (Fig. 3a,b). At the tip of the blades, where the α4 and α5 helices are connected, there is a partially disordered flexible loop that dips into the detergent/phospholipid shells, like a buoy floating on the membrane (Fig. 3a,b). At the center, E688, Q687, L686, Q339, T340, T341, Q342, T343, and R344 from both subunits form extensive side chain–side chain and side chain–main chain interactions (Fig. 3c). These electrostatic and hydrogen bonding networks create the symmetric dimer interface with a total area of 7,658 Å^2. Disruption of these interactions by mutations prohibited dimer formation (Fig. 3d–f). In particular, the T340A and E688A mutations markedly disrupted dimer assembly as revealed by FSEC (Fig. 3e,f) and the Q339A mutation had a modest effect (Fig. 3d), further emphasizing the importance of these residues in dimer formation.

OSCA channels have structural similarities with TMEM16 family proteins. Eleven transmembrane helices (M0 to M10), including the two membrane re-entering helices M7 and M8, form the transmembrane domain of each subunit. Using DALI search[28], we discovered that the majority of the transmembrane domains of *At*OSCA1.1 (M1 to M10) have structural similarities with TMEM16, a membrane protein family with diverse functions (Fig. 4a,b). The founding member of the TMEM16 family proteins, TMEM16A, was previously shown to constitute a calcium-activated chloride channel[29–31]. The cryo-EM structures of *m*TMEM16A are solved to a resolution of around 4 Å[32,33], which reveals the calcium-binding sites within the transmembrane domain. In *m*TMEM16A, the negatively charged residues E702 and E705 from M7, E734 and D738 from M8, and N651 and E654 from M6 cage two calcium ions (Fig. 4c) and these residues are highly conserved in TMEM16 family proteins[32,33]. In contrast, in the same region of *At*OSCA1.1, the negatively charged residues D524 and E532 on M6 and polar residue Q573 on M7 locate sparsely in 3D space (Fig. 4d). Whether *At*OSCA1.1 can bind calcium ions in this region remains elusive.

The putative location of OSCA channel pores. Structural and functional studies suggest that each TMEM16A subunit has one pore[34–36]. Our 20-Å low-pass filtered cryo-EM density map of *At*OSCA1.1 shows that there is one concave surface on each subunit (Supplementary Fig. 7a,b and Supplementary Video 1), indicating

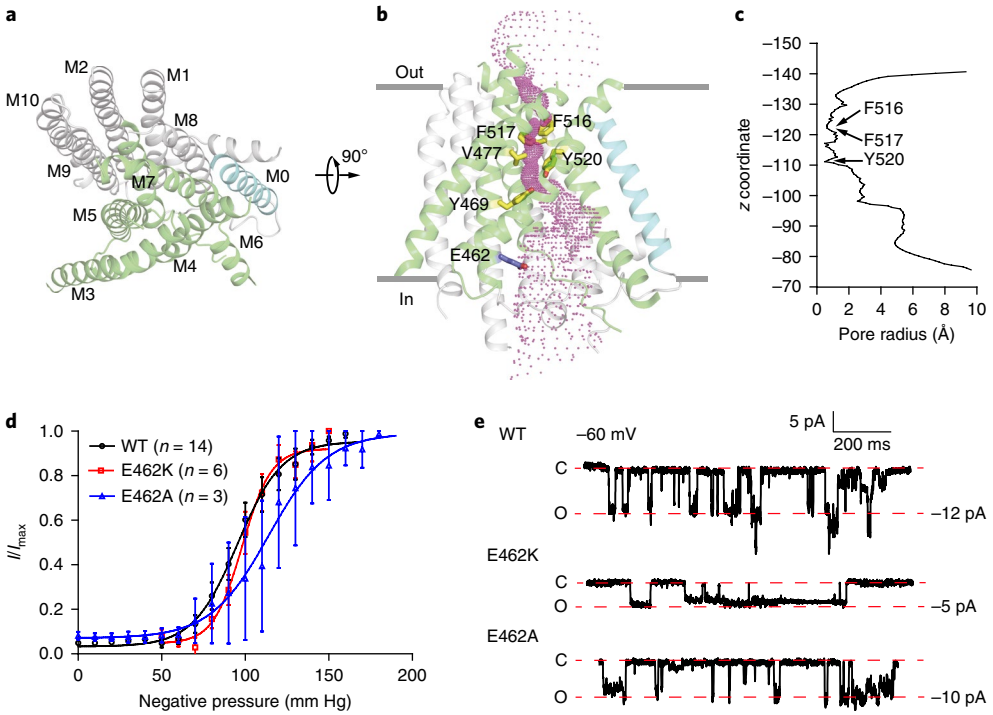

Fig. 5 | Transmembrane domain of *At*OSCA1.1 and putative ion permeation pathway. a, Top view of the transmembrane domain of one *At*OSCA1.1 subunit. Transmembrane helices that form the putative pore (M3, M4, M5, M6, and M7) are shown in green; M0 is shown in cyan; and the rest are shown in gray. **b**, Side view of the *At*OSCA1.1 transmembrane domain. The calculated pore profile of the putative *At*OSCA1.1 is indicated as purple dots. The hydrophobic residues F516, F517, and Y520 on M6, V477, and Y469 on M5 (in yellow) block the pore. The negatively charged residue E462 on M5 (in blue) is in a vestibule close to the cytoplasmic side. **c**, Pore radius of *At*OSCA1.1 along the *z* axis. The positions of the hydrophobic residues F516, F517, and Y520 on M6 that are blocking the pore are marked by arrows. **d**, The current–pressure relationship of wild-type *At*OSCA1.1 channel ($n = 14$), E462K ($n = 6$), and E462A ($n = 3$). The currents from each patch were normalized to I_{max}, the maximum current measured from the same inside-out patch. Errors bar indicate ±s.e.m.; n is the number of independent experiments. P_{50} is −95.4 ± 2.4 mm Hg for wild-type *At*OSCA1.1, −101.1 ± 3.9 mm Hg for E462K, and −114.0 ± 14.1 mm Hg for E462A. **e**, Representative single-channel currents of wild-type *At*OSCA1.1 (about −12 pA), E462K (about −5 pA), and E462A (about −10 pA) activated by a negative pressure of −60 mm Hg for *At*OSCA1.1 and E462K and −90 mm Hg for E462A at a holding potential of −60 mV.

that each individual transmembrane domain might possess solvent-accessible cavities that are not covered by detergent/phospholipid micelles. Moreover, the positions of the concave surfaces match the positions of the TMEM16A channel pore, which is formed by the transmembrane helices M3, M5, M7, M6, and M4[36,37]. On the basis of the features of our cryo-EM map and the structural similarity between *At*OSCA1.1 and the TMEM16A channel, we proposed that the pore of *At*OSCA1.1 is surrounded by the same sets of transmembrane helices as TMEM16A. Along the putative ion permeation pathway in *At*OSCA1.1, there is a vestibule close to the intracellular side, and the side chain of E462 on M5 protrudes into this vestibule (Fig. 5a,c). We found that the E462K mutation did not markedly shift the mechanosensitivity of *At*OSCA1.1, but dramatically reduced the major single-channel conductance from 200 to 83 pS (Fig. 5d,e and Supplementary Fig. 7c–f). In contrast, the E462A mutation (Fig. 5d,e and Supplementary Fig. 7c–f) did not have such effects. These results suggest that E462 is on the ion permeation pathway and supports our assignment of the ion channel pore. The calculated profile of the putative *At*OSCA1.1 pore shows that the hydrophobic residues F516, F517, and Y520 on M6 and V477 and Y469 on M5 form a thick gate that completely blocks the pore (Fig. 5a–c). As *At*OSCA1.1 can conduct organic gluconate ions (Fig. 1i), which have a diameter of 5.5 Å in the smallest cross-section[38], the narrowest constriction should be larger than 5.5 Å in diameter when the channel is fully open. Therefore, our *At*OSCA1.1 structure represents a non-conductive closed state, which is consistent with the fact that there is no osmolality or pressure mismatch between the intracellular and extracellular sides of the *At*OSCA1.1 channel in our cryo-EM sample preparation. The location of the pore is further supported by molecular dynamics simulations, in which we observed that water molecules could spontaneously form a continuous distribution within each subunit along the pathway as described above (Supplementary Fig. 8c). F516, F517, Y520, and V477 line the pore restriction site that is the most difficult for water molecules to access (Supplementary Fig. 8d). In contrast, the large cavity between the two subunits is filled with self-assembled lipid molecules throughout the simulations, and therefore neither water molecules nor ions can occupy the cavity (Supplementary Fig. 8a,b). These simulation results strongly suggest that the ion permeation pathway is within each subunit rather than through the central cavity between subunits, as water occupancy is usually a precondition for ion permeation to occur in channels. The continuous water profile was observed in a transient way and no ions were found to pass through the pore in the simulations, confirming that the structure of the *At*OSCA1.1 channel represents a non-conducive closed state. Interestingly, when surface tension was applied to the lipid bilayer, we observed a clear dilation of the OSCA channel pore in our molecular dynamics simulations. As depicted in Fig. 6a,c, the channel showed a very narrow pore around F516 to Y520 in our molecular dynamics simulations without any surface tension, which was very similar to that in the cryo-EM structure (Fig. 5b,c). Within 200 ns of applying a surface tension of 50 mN/m, the narrow pore region was widened to a more dilated state (Fig. 6b,c) in our all-atom molecular dynamics simulation. Meanwhile, the central cavity between the two subunits was still occluded by lipid molecules, confirming that the permeation pathway locates within each subunit rather than in between.

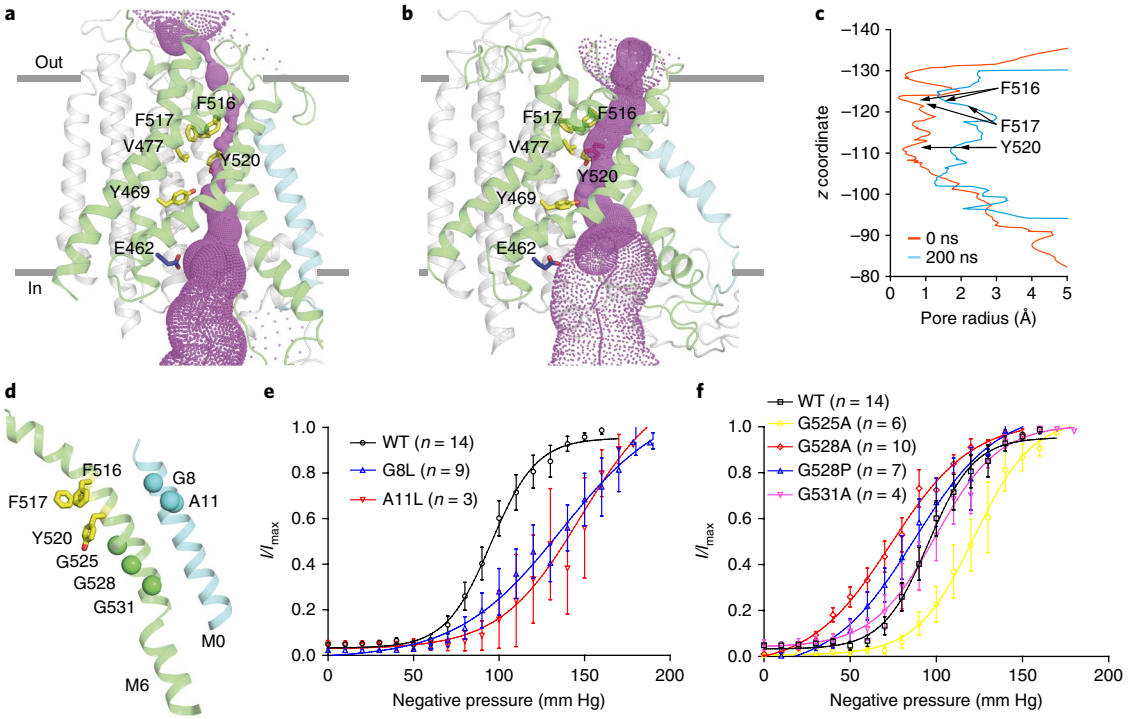

Fig. 6 | Pore dilation induced by surface tension and the role of the M0 and M6 helices in mechanosensation. a,b, Side view of the equilibrated structure in the molecular dynamics simulation without surface tension (**a**) and the structure after a 200-ns molecular dynamics simulation with 50 mN/m surface tension (**b**). The cartoon represents the OSCA structure, and the calculated pore profile is indicated as purple dots. **c**, The pore radius profiles of the OSCA channel before (red) and after (blue) a 200-ns molecular dynamics simulation with surface tension. **d**, F516, F517, and Y520 on M6 are shown as sticks. The Cα atoms of G525, G528, and G531 on M6 and G8 and A11 on M0 are shown as spheres. **e**, The current-pressure relationship of wild-type *At*OSCA1.1 channel ($n=14$), G8L ($n=9$), and A11L ($n=3$). The currents from each patch were normalized to I_{max}. P_{50} is -95.4 ± 2.4 mm Hg for wild-type *At*OSCA1.1, -136.6 ± 12.3 mm Hg for G8L, and -147.9 ± 16.2 mm Hg for A11L. Error bars indicate ±s.e.m.; n is the the number of independent experiments. **f**, The current-pressure relationship of G525A ($n=6$), G528A ($n=10$), G528P ($n=7$), and G531A ($n=4$). The currents from each patch were normalized to I_{max}. P_{50} is -122.1 ± 3.2 mm Hg for G525A, -73.8 ± 3.9 mm Hg for G528A, -87.3 ± 5.7 mm Hg for G528P, and -99.7 ± 4.0 mm Hg for G531A. Error bars indicate ±s.e.m.; n is the the number of independent experiments.

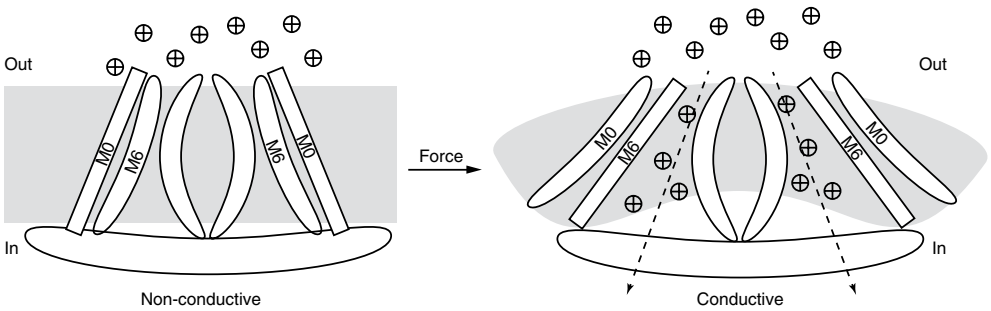

Fig. 7 | Proposed activation model of the *At*OSCA1.1 channel. The putative activation model of the OSCA channel is shown in a cartoon. Force or high-osmolality shock causes deformation of the local membrane, which may induce straightening of M6 and bending of M0 to drive channel pore opening.

OSCA channel activation involves conformational changes of the M0 and M6 helices. In TMEM16A, calcium activation induces conformational changes of the M6 helix, and G664A or G664P mutation shifted the EC_{50} curve to the lower calcium concentration, rendering the channel more easily activated by calcium[33]. In one of our 200-nS molecular dynamics simulations with surface tension, we observed a clear conformational change of the M6 helix along with dilation of the pore, indicating that this helix may be involved in the mechanosensitive gating for OSCA as well (Fig. 6b,c). In *At*OSCA1.1, three hydrophobic residues—F516, F517, and Y520—on the upper half of M6 block the ion permeation pathway, and there is bending of the M6 helix around G528 at the middle (Fig. 6d). We mutated G528 to alanine or proline and discovered that these mutations shift the P_{50} curve to a lower pressure (Fig. 6f), suggesting that channel activation might involve straightening of M6 around G528 to relieve the blockage of the ion channel pore. In contrast, the G525A and G531A mutations on M6 do not have such an effect (Fig. 6f). Compared to TMEM16 family proteins, OSCA channels possess an additional M0 helix that interacts with M6 (Fig. 6d). To test whether this additional M0 is involved in mechanosensation, we mutated residues on

M0 of *At*OSCA1.1 into the corresponding residues of *At*OSCA3.1, which has a higher activation pressure threshold than *At*OSAC1.1 (Supplementary Fig. 6). We found that replacement of G8 and A11, which have no or small side chains, into bulkier leucine residues can shift the P_{50} curve to a higher pressure (Fig. 6e). Interestingly, G8 and A11 on the upper region of M0 do not interact with M6 directly (Fig. 6d), and leucine replacements can be accommodated in the current closed-state structure, which suggests that these leucine residues might be in contact with and inhibit the conformational change of adjacent M6 during channel activation.

Discussion

Our study showed that *At*OSCA1.1 and *At*OSCA3.1 constitute novel pressure-activated ion channels. The dimeric architectures and transmembrane domain structures of *At*OSCA1.1 and *At*OSCA3.1 are reminiscent of TMEM16 family channels, and they also have similar pore locations. The fact that the cone-shaped lipid LPC can activate the channel suggests that the OSCA channels might directly sense force from lipid, akin to the well-studied MscL channel[14]. For mechanosensitive membrane proteins, the cross-sectional area of the transmembrane domain should be expanded on activation[39]. We speculate that membrane tension generated by applied pressure can induce a conformational change in the transmembrane domains of OSCA. These conformational changes will result in increased cross-sectional area of the transmembrane domain and opening of the ion channel pore (Fig. 7). OSCA family proteins are widely distributed among all eukaryotic kingdoms. Our results provide a structural basis to understand how these evolutionarily conserved proteins work.

Online content

Any methods, additional references, Nature Research reporting summaries, source data, statements of data availability and associated accession codes are available at https://doi.org/10.1038/s41594-018-0117-6.

Received: 1 March 2018; Accepted: 24 July 2018;
Published online: 06 September 2018

References

1. Booth, I. R. & Blount, P. The MscS and MscL families of mechanosensitive channels act as microbial emergency release valves. *J. Bacteriol.* **194**, 4802–4809 (2012).
2. Walker, R. G., Willingham, A. T. & Zuker, C. S. A *Drosophila* mechanosensory transduction channel. *Science* **287**, 2229–2234 (2000).
3. Yan, Z. et al. *Drosophila* NOMPC is a mechanotransduction channel subunit for gentle-touch sensation. *Nature* **493**, 221–225 (2013).
4. Zhang, W., Yan, Z., Jan, L. Y. & Jan, Y. N. Sound response mediated by the TRP channels NOMPC, NANCHUNG, and INACTIVE in chordotonal organs of *Drosophila* larvae. *Proc. Natl. Acad. Sci. USA* **110**, 13612–13617 (2013).
5. Lehnert, B. P., Baker, A. E., Gaudry, Q., Chiang, A. S. & Wilson, R. I. Distinct roles of TRP channels in auditory transduction and amplification in *Drosophila*. *Neuron* **77**, 115–128 (2013).
6. Maingret, F., Fosset, M., Lesage, F., Lazdunski, M. & Honore, E. TRAAK is a mammalian neuronal mechano-gated K^+ channel. *J. Biol. Chem.* **274**, 1381–1387 (1999).
7. Wu, J., Lewis, A. H. & Grandl, J. Touch, tension, and transduction—the function and regulation of piezo ion channels. *Trends Biochem. Sci.* **42**, 57–71 (2017).
8. Basu, D. & Haswell, E. S. Plant mechanosensitive ion channels: an ocean of possibilities. *Curr. Opin. Plant Biol.* **40**, 43–48 (2017).
9. Jin, P. et al. Electron cryo-microscopy structure of the mechanotransduction channel NOMPC. *Nature* **547**, 118–122 (2017).
10. Zhang, W. et al. Ankyrin repeats convey force to gate the NOMPC mechanotransduction channel. *Cell* **162**, 1391–1403 (2015).
11. Martinac, B., Adler, J. & Kung, C. Mechanosensitive ion channels of *E. coli* activated by amphipaths. *Nature* **348**, 261–263 (1990).
12. Kung, C. A possible unifying principle for mechanosensation. *Nature* **436**, 647–654 (2005).
13. Perozo, E., Cortes, D. M., Sompornpisut, P., Kloda, A. & Martinac, B. Open channel structure of MscL and the gating mechanism of mechanosensitive channels. *Nature* **418**, 942–948 (2002).
14. Perozo, E., Kloda, A., Cortes, D. M. & Martinac, B. Physical principles underlying the transduction of bilayer deformation forces during mechanosensitive channel gating. *Nat. Struct. Biol.* **9**, 696–703 (2002).
15. Sukharev, S. I., Blount, P., Martinac, B., Blattner, F. R. & Kung, C. A large-conductance mechanosensitive channel in *E. coli* encoded by *mscL* alone. *Nature* **368**, 265–268 (1994).
16. Brohawn, S. G., Campbell, E. B. & MacKinnon, R. Physical mechanism for gating and mechanosensitivity of the human TRAAK K^+ channel. *Nature* **516**, 126–130 (2014).
17. Brohawn, S. G., Su, Z. & MacKinnon, R. Mechanosensitivity is mediated directly by the lipid membrane in TRAAK and TREK1 K^+ channels. *Proc. Natl. Acad. Sci. USA* **111**, 3614–3619 (2014).
18. Syeda, R. et al. Piezo1 channels are inherently mechanosensitive. *Cell Rep.* **17**, 1739–1746 (2016).
19. Cox, C. D. et al. Removal of the mechanoprotective influence of the cytoskeleton reveals PIEZO1 is gated by bilayer tension. *Nat. Commun.* **7**, 10366 (2016).
20. Osakabe, Y., Osakabe, K., Shinozaki, K. & Tran, L. S. Response of plants to water stress. *Front. Plant Sci.* **5**, 86 (2014).
21. Yuan, F. et al. OSCA1 mediates osmotic-stress-evoked Ca^{2+} increases vital for osmosensing in *Arabidopsis*. *Nature* **514**, 367–371 (2014).
22. Hou, C. et al. DUF221 proteins are a family of osmosensitive calcium-permeable cation channels conserved across eukaryotes. *Cell Res.* **24**, 632–635 (2014).
23. Vasquez, R. J., Howell, B., Yvon, A. M., Wadsworth, P. & Cassimeris, L. Nanomolar concentrations of nocodazole alter microtubule dynamic instability in vivo and in vitro. *Mol. Biol. Cell* **8**, 973–985 (1997).
24. Kiyosue, T., Yamaguchi-Shinozaki, K. & Shinozaki, K. Cloning of cDNAs for genes that are early-responsive to dehydration stress (ERDs) in *Arabidopsis thaliana* L.: identification of three ERDs as HSP cognate genes. *Plant Mol. Biol.* **25**, 791–798 (1994).
25. Kawate, T. & Gouaux, E. Fluorescence-detection size-exclusion chromatography for precrystallization screening of integral membrane proteins. *Structure* **14**, 673–681 (2006).
26. Guo, J. et al. Structure of the voltage-gated two-pore channel TPC1 from *Arabidopsis thaliana*. *Nature* **531**, 196–201 (2016).
27. Kintzer, A. F. & Stroud, R. M. Structure, inhibition and regulation of two-pore channel TPC1 from *Arabidopsis thaliana*. *Nature* **531**, 258–262 (2016).
28. Holm, L. & Rosenstrom, P. Dali server: conservation mapping in 3D. *Nucleic Acids Res.* **38**, W545–W549 (2010).
29. Caputo, A. et al. TMEM16A, a membrane protein associated with calcium-dependent chloride channel activity. *Science* **322**, 590–594 (2008).
30. Schroeder, B. C., Cheng, T., Jan, Y. N. & Jan, L. Y. Expression cloning of TMEM16A as a calcium-activated chloride channel subunit. *Cell* **134**, 1019–1029 (2008).
31. Yang, Y. D. et al. TMEM16A confers receptor-activated calcium-dependent chloride conductance. *Nature* **455**, 1210–1215 (2008).
32. Dang, S. et al. Cryo-EM structures of the TMEM16A calcium-activated chloride channel. *Nature* **552**, 426–429 (2017).
33. Paulino, C., Kalienkova, V., Lam, A. K. M., Neldner, Y. & Dutzler, R. Activation mechanism of the calcium-activated chloride channel TMEM16A revealed by cryo-EM. *Nature* **552**, 421–425 (2017).
34. Jeng, G., Aggarwal, M., Yu, W. P. & Chen, T. Y. Independent activation of distinct pores in dimeric TMEM16A channels. *J. Gen. Physiol.* **148**, 393–404 (2016).
35. Lim, N. K., Lam, A. K. & Dutzler, R. Independent activation of ion conduction pores in the double-barreled calcium-activated chloride channel TMEM16A. *J. Gen. Physiol.* **148**, 375–392 (2016).
36. Paulino, C. et al. Structural basis for anion conduction in the calcium-activated chloride channel TMEM16A. *eLife* **6**, e26232 (2017).
37. Peters, C. J. et al. Four basic residues critical for the ion selectivity and pore blocker sensitivity of TMEM16A calcium-activated chloride channels. *Proc. Natl. Acad. Sci. USA* **112**, 3547–3552 (2015).
38. Duszyk, M., French, A. S. & Man, S. F. The 20-pS chloride channel of the human airway epithelium. *Biophys. J.* **57**, 223–230 (1990).
39. Haswell, E. S., Phillips, R. & Rees, D. C. Mechanosensitive channels: what can they do and how do they do it? *Structure* **19**, 1356–1369 (2011).

Acknowledgements

We thank all the Chen laboratory members for support, especially M. Wang and Y. Niu for help with manuscript preparation, and D. Ding, W. Guo, Q. Tang, and S. Qiu for help with EM data collection. We thank C. Zhang for sharing electrophysiology equipments, S. Zhong at Peking University for providing *Arabidopsis thaliana* total cDNA, and D. Ren at the Department of Biology, University of Pennsylvania for providing mouse TPC1 cDNA. Cryo-EM data collection was supported by the National Center for Protein Science (Shanghai) with the assistance of L. Kong and Z. Fu, the Center for Biological Imaging, the Electron Microscopy Laboratory and Cryo-EM platform of Peking University with the assistance of X. Li and the Center for Biological Imaging, Institute

of Biophysics, Chinese Academy of Science with the assistance of Z. Guo. Part of the structural computation and molecular dynamics simulation was performed on the High-performance Computing Platform of Peking University and the Computing Platform of the Center for Life Science, Peking University. The work is supported by grants from the Ministry of Science and Technology of China (National Key R&D Program of China, grant no. 2016YFA0502004 to L.C., grant no. 2016YFA0500401 to C.S., grant nos. 2017YFA0103900 and 2016YFA0502800 to Z.Y.), National Natural Science Foundation of China (grant nos. 31622021 and 31521062 to L.C., grant no. 31571083 to Z.Y.), the Program for Professor of Special Appointment (Eastern Scholar of Shanghai, grant no. TP2014008 to Z.Y.), the Shanghai Rising-Star Program (grant no. 14QA1400800 to Z.Y.), the Young Thousand Talents Program of China to L.C., C.S., and Z.Y., and the China Postdoctoral Science Foundation (grant nos. 2016M600856 and 2017T100014 to J.-X.W.). J.-X.W. is supported by the Peking University Boya Postdoctoral Fellowship and the postdoctoral foundation of the Peking-Tsinghua Center for Life Sciences, Peking University.

Author contributions

M.Z. and L.C. conceived the project. Z.Y., C.S., and L.C. designed experiments. M.Z., C.P., and Z.Y. performed electrophysiology experiments. M.Z., J.-X.W., F.Y., and L.C. performed mutagenesis and FSEC experiments. Y.K. and J.-X.W. performed the calcium imaging experiments. D.W. and C.S. performed molecular dynamics simulations. M.Z. prepared the cryo-EM sample. M.Z., J.-X.W., Y.K., and L.C. collected cryo-EM data. M.Z. and L.C. performed image processing and analyzed EM data. L.C. built the model and wrote the manuscript draft. All authors contributed to the manuscript preparation.

Competing interests

The authors declare no competing interests.

Additional information

Supplementary information is available for this paper at https://doi.org/10.1038/s41594-018-0117-6.

Reprints and permissions information is available at www.nature.com/reprints.

Correspondence and requests for materials should be addressed to Z.Y. or C.S. or L.C.

Publisher's note: Springer Nature remains neutral with regard to jurisdictional claims in published maps and institutional affiliations.

Methods

Cell lines. Sf9 cells were from Thermo Fisher Scientific and cultured in Sf-900 III SFM medium at 27 °C. FreeStyle 293-F cells were from Thermo Fisher Scientific. FreeStyle 293-F suspension cells were cultured in FreeStyle 293 medium supplemented with 1% FBS at 37 °C with 6% CO_2 and 70% humidity. Cells were routinely tested for mycoplasma contamination and were negative.

Fluorescence-detection size-exclusion chromatography. The cDNA for *At*OSCA1.1 (UniprotKB Q9XEA1), *At*OSCA3.1 (UniprotKB Q9C8G5), and *m*TPC1 (UniprotKB Q9EQJ0) was cloned into a modified C-terminally GFP-tagged BacMam expression vector, which also contains a His_8 tag after GFP[40]. FreeStyle 293-F cells transfected by *At*OSCA1.1-CGFP and *m*TPC1 were harvested and solubilized in Tris-buffered saline (TBS; 20 mM Tris pH 8.0 and 150 mM NaCl), 1% maltose neopentyl glycol (MNG), and 0.1% cholesteryl hemisuccinate (CHS) for 0.5 h at 4 °C, then centrifuged at 15,000*g* to remove unsolubilized cells. Supernatants were centrifuged at 40,000 r.p.m. in a TLA55 rotor for 30 min to remove unsolublized membrane. Supernatants were injected onto a Superose 6 increase 5/150 column (GE Healthcare), pre-equilibrated with TBS and 10 µM MNG, and detected by a fluorescence detector (excitation 488 nm and emission 520 nm for GFP signal, excitation 280 nm and emission 335 nm for tryptophan signal)[25]. Mutant channels were analyzed in the same manner as wild-type channels.

Calcium imaging. FreeStyle 293-F cells grown in 293TI medium were transfected with plasmid DNA using polyethylenimine (PEI) reagents and seeded on poly-D-lysine-coated coverslips. After 18–24 h, cells were loaded with 4 µM Rhod-2AM supplemented with 0.02% pluronic F127 in a buffer containing 10 mM HEPES (pH 7.4), 130 mm *N*-methyl-D-glucamine (NMDG), 3 mM KCl, 2 mM $CaCl_2$, 0.6 mM $MgCl_2$, and 10 mM glucose, and incubated at 37 °C for 5 min. Ca^{2+} imaging was performed on a PerkinElmer UltraView Vox spinning-disk confocal microscope using an excitation/emission wavelength of 561/600 nm (for the Rhod signal) and 488/524 nm (for the GFP signal). A final concentration of 650 mM sorbitol was added to the bath solution and the Rhod2/GFP signal was collected. For data analysis, 20–30 cells were selected based on the GFP fluorescence. Rhod2 fluorescence (F) was background-corrected and normalized to the resting fluorescence (F_0). All data collection and analysis were carried out using Volocity software.

Electrophysiology. FreeStyle 293-F cells were transfected with *At*OSCA1.1-CGFP, *At*OSCA3.1-CGFP, *Hs*TRAAK, or CGFP empty plasmid and incubated for 24–36 h before recording. Inside-out patches were performed in symmetrical solution. The bath and pipette solutions were both 10 mM HEPES (pH 7.2) and 150 mM potassium gluconate (KGlu). For ion-selectivity experiments, the pipette solution was unchanged and the bath solution was replaced by 10 mM HEPES (pH 7.2), 30 mM KGlu, and 240 mM sucrose or 10 mM HEPES (pH 7.2) and 150 mM KCl. Junction potentials were calculated based on the solution composition and corrected before plotting. Permeability ratios were calculated using the following Goldman–Hodgkin–Katz equation: $E_{rev} = (RT/F) \ln((P_K[K]_o + P_X[X]_i)/(P_K[K]_i + P_X[X]_o))$, where X is the gluconate or chloride ion.

The pipettes were pulled by a vertical electrode drawing instrument (PC-10), and the pipette resistance was 8–10 MΩ. Currents were recorded at −60 mV using an Axopatch 700B amplifier at a sampling rate of 20 kHz and filtered at 5 kHz (Digidata 1440 A, Molecular Devices). Negative pressure in the pipette was applied using a Suction Control Pro unit (Nanion) with a stepwise protocol through Clampex software. We used an I/I_{max} versus negative pressure curve approach for evaluating mechanosensitivity, where I_{max} is the maximum current measured from the patch excised in the inside-out patch clamp setting[14,41]. All recordings were performed at 22 °C. Data were then analyzed by pClamp10.4 software. All data were acquired from at least three independent cells.

Protein expression and purification. Baculovirus was generated from the DH10MultiBacMam bacteria strain[42] and sf9 cells according to a standard Bac-to-Bac protocol. For large-scale expression, FreeStyle 293-F cells (grown in FreeStyle 293 medium with 1% FBS and 5% CO_2 at 37 °C) in suspension were grown to a density of 3.0×10^6 cells/ml and then infected by baculovirus. 10 mM sodium butyrate was added 12 h post-infection, and the temperature was lowered to 30 °C for protein expression. Cells were harvested 72 h post-infection and broken by sonication in lysis buffer (20 mM Tris pH 7.5, 2 mM $MgCl_2$, 200 mM NaCl, 20% glycerol), supplied with 1 µg/ml aprotinin, 1 µg/ml leupeptin, 1 µg/ml pepstatin, and 1 mM phenylmethylsulfonyl fluoride. Unbroken cells and cell debris were removed by centrifugation at 8,000 r.p.m. for 20 min. Supernatant was centrifuged at 40,000 r.p.m. for 1 h in a Ti45 rotor (Beckman). Membrane pellets were harvested and frozen at −80 °C until use.

For purification, membrane pellets were homogenized in TBS and then solubilized in TBS, 1% MNG, and 0.1% CHS for 1 h at 4 °C. Unsolubilized materials were removed by centrifugation at 40,000 r.p.m. for 30 min in a Ti45 rotor. Supernatant was loaded onto TALON resin (Clontech) by gravity flow. Resin was further washed with 10 column volumes of wash buffer (TBS, 0.025% MNG, and 10 mM imidazole), and protein was eluted with an elution buffer (TBS, 0.025% MNG, and 250 mM imidazole). The C-terminal GFP tag of eluted protein was removed by H3CV protease cleavage for 3 h at 4 °C. The protein was further concentrated by a 100-kDa cutoff concentrator (Millipore) and loaded onto a Superose 6 increase 10/300 column (GE Healthcare) running in TBS and 0.1% digitonin. Peak fractions were combined and concentrated to around 9 mg/ml of *At*OSCA1.1 and 5 mg/ml of *At*OSCA3.1 for cryo-EM sample preparation.

EM sample preparation. Cryo-EM grids were prepared with Vitrobot Mark IV (FEI). GiG R1/1 holey carbon grids were glow-discharged for 60 s using 50% argon and 50% oxygen. Approximately 2.5-µl aliquots of the sample were applied to the glow-discharged grid, and then the grid was blotted with a blotting force of level 2 for 5 s at 100% humidity (22 °C) before being plunge-frozen in liquid ethane.

Data collection. Cryo-EM data for *At*OSCA1.1 were collected on a Titan Krios microscope (FEI) equipped with a cesium corrector operated at 300 kV. Videos were acquired with Serial EM software on a K2 camera in super-resolution mode with pixel size 0.5 Å per pixel at the object plane and with defocus ranging from −1.5 µm to −3.5 µm. The dose rate on the sample was 8 $e^- s^{-1} Å^{-2}$, and each video was 6.25 s long and dose-fractioned into 50 frames with 125 ms for each frame. Total exposure was 50 $e^- Å^{-2}$. Cryo-EM data for *At*OSCA3.1 were collected on a Titan Krios microscope (FEI) operated at 300 kV. Videos were acquired with EPU software on a K2 camera with a Quantum energy filter operated at a slit width of 20 eV. Videos were collected in counting mode with pixel size 1.055 Å per pixel at the object plane and with defocus ranging from −1.5 µm to −3.5 µm. The dose rate on the sample was 5.235 $e^- s^{-1} Å^{-2}$, and each video was 10 s long and dose-fractioned into 40 frames with 250 ms for each frame. Total exposure was 52 $e^- Å^{-2}$.

Image processing. 2,210 videos of *At*OSCA1.1 were motion-corrected, exposure-filtered, and binned with MotionCor2 with 5 × 5 patches, producing summed and dose-weighted micrographs with pixel size 1 Å per pixel[43]. CTF (contrast transfer function) models of dose-weighted micrographs were determined using gctf[44]. Around 1,000 particles were manually picked, and 2D classification was performed using GPU-accelerated Relion 2.0[45]. The resulting 2D class averages were used as the template for auto-picking with Relion 2.0. 415,262 auto-picked particles were extracted from dose-weighted micrographs with a binning factor of 2 (2 Å per pixel) and subjected to repeated 2D classification. The initial model was generated using cryoSPARC from particles after cleaning up by 2D classification[46]. The initial model was low-pass filtered to 30 Å for 3D classification in Relion 2.0. Particles from 3D classes with visible secondary structure were centered and re-extracted from the original micrographs without binning (1 Å per pixel). Re-extracted particles were subjected to 3D auto-refinement with Relion 2.0 and the reconstruction reached 3.82 Å after postprocessing. Applying a detergent-free soft mask modestly improved the resolution to 3.76 Å. Further reference-free 3D classification ($k = 4$ classes) was carried out with cryoSPARC using an ab initio reconstruction algorithm. 115,692 particles were selected for subsequent homogenous refinement with *C*2 symmetry and the resolution reached 3.52 Å with an auto-tightened mask determined by cryoSPARC automatically. Resolution estimation was based on gold-standard FSC 0.143, after correction for mask effects[47]. The final map was sharpened with B factor −159.0 $Å^2$ determined by cryoSPARC. The local resolution map was calculated using ResMap[48]. The *At*OSCA3.1 dataset was processed with a similar procedure, except for the fact that a Relion 2.0 pipeline was used.

Model building. EM builder[49] was used to build a de novo model of *At*OSCA1.1 according to the 3.52-Å map. The ab initio partial model was manually rebuilt and extended with Coot[50]. The assignment of a sequence was aided by locating the density of residues with bulky side chains. Due to poorly resolved densities of flexible regions, residues 267–274 were built as polyalanine and residues 1–3, 43–69, 125–155, 276–290, 403–421, and 717–772 were omitted in the final model. Refinement was against one of the sharpened and masked half-maps ("work" in Supplementary Fig. 4c) with phenix.real_space_refine[51] and Refmac5[52] using scripts provided by A. Brown. Secondary structure restrains were applied throughout the refinement cycles. The other half-map ("free" in Supplementary Fig. 4c) was used to assess overfitting. The *At*OSCA3.1 structure was homology modeled using the *At*OSCA1.1 structure by SWISS-MODEL[53] and refined against the full map of *At*OSCA3.1. The permeation pathway was calculated by HOLE[54]. Figures were prepared with Pymol (Schrödinger) or Chimera[55].

Coarse-grained molecular dynamics simulations. All the molecular dynamics simulations were performed with Gromacs 5.1.3[56]. The cryo-EM structure of *At*OSCA1.1 was used as the initial structure for coarse-grained self-assembly molecular dynamics simulations. We put the structure into a simulation box in which water and 1-palmitoyl-2-oleoyl-*sn*-glycero-3-phosphocholine (POPC) molecules were placed randomly. After tens of nanosecond free equilibration simulations, the POPC molecules spontaneously assembled around the OSCA structure to form a bilayer and some POPC molecules spontaneously occupied the cavity between the two subunits of OSCA. The coarse-grained molecular dynamics was performed for five independent repeats with the MARTINI force field[57] with elastic network. Before production molecular dynamics simulations,

we equilibrated the system to remove bad contacts and reach the desired target conditions. First, the system was energy minimized for 5,000 steps, and then 10-ns NVT (canonical ensemble) equilibration was performed with a time step of 20 fs. After equilibration, we ran five 200-ns independent simulations with a time step of 20 fs under the NPT ensemble (isothermal-isobaric ensemble). The V-rescale algorithm with a coupling time of 1.0 ps was used to maintain the temperature at 310 K[58]. The Berendsen thermostat with a coupling time of 1.0 ps was used to maintain the pressure at 1.0 bar[59]. The electrostatic interactions were calculated with the reaction-field method. The van der Waals interaction was cut off at 1.1 nm.

All-atom molecular dynamics simulations. We picked one of the final frames of the coarse-grained simulations as the template to build the all-atom (AA) model system. The procedure involves two steps: (i) we utilized the backward tool[60] to transform the OSCA + POPC + water system obtained from the coarse-grained simulations above to the AA model. (ii) We replaced the backward-generated *At*OSCA1.1 structure with the cryo-EM *At*OSCA1.1 structure, whose missing residues were filled and refined with Modeller[61]. We used mdrun-membed in Gromacs to remove the lipid and water molecules that overlapped with *At*OSCA1.1. This AA system was then used to perform molecular dynamics simulations with the AMBER99sb-ildn force field[62]. The Slipid parameters of POPC[63,64] were incorporated into the AMBER99sb-ildn force field and used for our AA molecular dynamics simulations. Na^+ and Cl^- were added in a TIP3P water box to get a neutral system. After 10,000 steps of energy minimization, the system was equilibrated within the NVT and NPT ensembles. We performed 0.5-ns NVT equilibration with a time step of 2 fs, and then the system was equilibrated for 5 ns in the NPT ensemble with a 1,000 kJ/mol/nm^2 position restraint on all OSCA heavy atoms. Subsequently, we performed 15-ns NPT equilibration with restraints on all the Cα in OSCA except for the loops built by Modeller, to further refine the loop conformations before production simulations. The long-range electrostatic interactions were calculated with Particle-Mesh Ewald[65]. The reference temperature was 310 K. Semi-isotropic pressure coupling was used to maintain the pressure at 1.0 bar. The van der Waals cutoff was 1.0 nm. The Berendsen method was used for temperature coupling and pressure coupling during the equilibration[59]. After the system was well equilibrated to the desired temperature and pressure, we released the position restraints and ran multiple independent 200-ns production molecular dynamics simulations under the NPT ensemble, with V-rescale temperature coupling[66] and Parrinello–Rahman pressure coupling[67,68].

Molecular dynamics simulations with surface tension. After performing a 15-ns NPT equilibration, we took the equilibrated system and applied surface tension on the bilayer surface (*x*–*y* plane) to investigate whether the OSCA channel can respond to the mechanical stimuli. In these simulations, we utilized the 'surface-tension' method as implemented in Gromacs software together with Berendsen pressure coupling[57,65,66]. We set the surface tension to 50 mN/m in the *x*–*y* plane and maintained the pressure in the *z* direction at 1.0 bar. All other simulation parameters were the same as described above. Three independent 200-ns molecular dynamics simulations with surface tension were performed.

Reporting Summary. Further information on research design is available in the Nature Research Reporting Summary linked to this article.

Data availability

The modeled atomic coordinates have been deposited in PDB with accession codes 5YD1 (AtOSCA1.1) and 5Z1F (AtOSCA3.1). In addition, EM maps have been deposited in EMDB with accession codes EMD-6822 (AtOSCA1.1) and EMD-6875 (*At*OSCA3.1). All other source data are available from the corresponding authors upon reasonable request.

References

40. Goehring, A. et al. Screening and large-scale expression of membrane proteins in mammalian cells for structural studies. *Nat. Protoc.* **9**, 2574–2585 (2014).
41. Doerner, J. F., Febvay, S. & Clapham, D. E. Controlled delivery of bioactive molecules into live cells using the bacterial mechanosensitive channel MscL. *Nat. Commun.* **3**, 990 (2012).
42. Mansouri, M. et al. Highly efficient baculovirus-mediated multigene delivery in primary cells. *Nat. Commun.* **7**, 11529 (2016).
43. Zheng, S. Q. et al. MotionCor2: anisotropic correction of beam-induced motion for improved cryo-electron microscopy. *Nat. Methods* **14**, 331–332 (2017).
44. Zhang, K. Gctf: real-time CTF determination and correction. *J. Struct. Biol.* **193**, 1–12 (2016).
45. Kimanius, D., Forsberg, B. O., Scheres, S. H. & Lindahl, E. Accelerated cryo-EM structure determination with parallelisation using GPUs in RELION-2. *eLife* **5**, e18722 (2016).
46. Punjani, A., Rubinstein, J. L., Fleet, D. J. & Brubaker, M. A. cryoSPARC: algorithms for rapid unsupervised cryo-EM structure determination. *Nat. Methods* **14**, 290–296 (2017).
47. Chen, S. et al. High-resolution noise substitution to measure overfitting and validate resolution in 3D structure determination by single particle electron cryomicroscopy. *Ultramicroscopy* **135**, 24–35 (2013).
48. Kucukelbir, A., Sigworth, F. J. & Tagare, H. D. Quantifying the local resolution of cryo-EM density maps. *Nat. Methods* **11**, 63–65 (2014).
49. Zhou, N., Wang, H. & Wang, J. EMBuilder: a template matching-based automatic model-building program for high-resolution cryo-electron microscopy maps. *Sci. Rep.* **7**, 2664 (2017).
50. Emsley, P., Lohkamp, B., Scott, W. G. & Cowtan, K. Features and development of Coot. *Acta Crystallogr. D Biol. Crystallogr.* **66**, 486–501 (2010).
51. Adams, P. D. et al. PHENIX: a comprehensive Python-based system for macromolecular structure solution. *Acta Crystallogr. D Biol. Crystallogr.* **66**, 213–221 (2010).
52. Nicholls, R. A., Long, F. & Murshudov, G. N. Low-resolution refinement tools in REFMAC5. *Acta Crystallogr. D Biol. Crystallogr.* **68**, 404–417 (2012).
53. Biasini, M. et al. SWISS-MODEL: modelling protein tertiary and quaternary structure using evolutionary information. *Nucleic Acids Res.* **42**, W252–W258 (2014).
54. Smart, O. S., Neduvelil, J. G., Wang, X., Wallace, B. A. & Sansom, M. S. HOLE: a program for the analysis of the pore dimensions of ion channel structural models. *J. Mol. Graph.* **14**, 354–360 (1996).
55. Pettersen, E. F. et al. UCSF Chimera—a visualization system for exploratory research and analysis. *J. Comput. Chem.* **25**, 1605–1612 (2004).
56. Abraham, M. J. et al. GROMACS: high performance molecular simulations through multi-level parallelism from laptops to supercomputers. *SoftwareX* **2**, 19–25 (2015).
57. Marrink, S. J., Risselada, H. J., Yefimov, S., Tieleman, D. P. & De Vries, A. H. The MARTINI force field: coarse grained model for biomolecular simulations. *J. Phys. Chem. B* **111**, 7812–7824 (2007).
58. Bussi, G., Donadio, D. & Parrinello, M. Canonical sampling through velocity rescaling. *J. Chem. Phys.* **126**, 014101 (2007).
59. Berendsen, C. et al. Molecular dynamics with coupling to an external bath. *J. Chem. Phys.* **81**, 3684–3690 (1984).
60. Wassenaar, T. A., Pluhackova, K., Böckmann, R. A., Marrink, S. J. & Tieleman, D. P. Going backward: a flexible geometric approach to reverse transformation from coarse grained to atomistic models. *J. Chem. Theory Comput.* **10**, 676–690 (2014).
61. Šali, A. & Blundell, T. L. Comparative protein modelling by satisfaction of spatial restraints. *J. Mol. Biol.* **234**, 779–815 (1993).
62. Lindorff-Larsen, K. et al. Improved side-chain torsion potentials for the Amber ff99SB protein force field. *Proteins* **78**, 1950–1958 (2010).
63. Jämbeck, J. P. M. & Lyubartsev, A. P. An extension and further validation of an all-atomistic force field for biological membranes. *J. Chem. Theory Comput.* **8**, 2938–2948 (2012).
64. Jämbeck, J. P. M. & Lyubartsev, A. P. Derivation and systematic validation of a refined all-atom force field for phosphatidylcholine lipids. *J. Phys. Chem. B* **116**, 3164–3179 (2012).
65. Darden, T., York, D. & Pedersen, L. Particle mesh Ewald: an *N*log(*N*) method for Ewald sums in large systems. *J. Chem. Phys.* **98**, 10089–10092 (1993).
66. Bussi, G. Canonical sampling through velocity rescaling. *J. Chem. Phys.* **126**, 014101 (2007).
67. Parrinello, M. & Rahman, A. Polymorphic transitions in single crystals: a new molecular dynamics method. *J. Appl. Phys.* **52**, 7182–7190 (1981).
68. Nosé, S. & Klein, M. L. Constant pressure molecular dynamics for molecular systems. *Mol. Phys.* **50**, 1055–1076 (1983).

nature research

Corresponding author(s): Lei Chen, Chen Song and Zhiqiang Yan

Reporting Summary

Nature Research wishes to improve the reproducibility of the work that we publish. This form provides structure for consistency and transparency in reporting. For further information on Nature Research policies, see Authors & Referees and the Editorial Policy Checklist.

Statistical parameters

When statistical analyses are reported, confirm that the following items are present in the relevant location (e.g. figure legend, table legend, main text, or Methods section).

n/a	Confirmed	
☐	☒	The exact sample size (*n*) for each experimental group/condition, given as a discrete number and unit of measurement
☐	☒	An indication of whether measurements were taken from distinct samples or whether the same sample was measured repeatedly
☒	☐	The statistical test(s) used AND whether they are one- or two-sided *Only common tests should be described solely by name; describe more complex techniques in the Methods section.*
☒	☐	A description of all covariates tested
☒	☐	A description of any assumptions or corrections, such as tests of normality and adjustment for multiple comparisons
☐	☒	A full description of the statistics including central tendency (e.g. means) or other basic estimates (e.g. regression coefficient) AND variation (e.g. standard deviation) or associated estimates of uncertainty (e.g. confidence intervals)
☒	☐	For null hypothesis testing, the test statistic (e.g. *F*, *t*, *r*) with confidence intervals, effect sizes, degrees of freedom and *P* value noted *Give P values as exact values whenever suitable.*
☒	☐	For Bayesian analysis, information on the choice of priors and Markov chain Monte Carlo settings
☒	☐	For hierarchical and complex designs, identification of the appropriate level for tests and full reporting of outcomes
☒	☐	Estimates of effect sizes (e.g. Cohen's *d*, Pearson's *r*), indicating how they were calculated
☐	☒	Clearly defined error bars *State explicitly what error bars represent (e.g. SD, SE, CI)*

Our web collection on statistics for biologists may be useful.

Software and code

Policy information about availability of computer code

Data collection	Serial EM, pClamp.
Data analysis	RELION, cryoSPARC, EM builder, Coot, Chimera, Pymol, Volocity, Phenix, Gromacs, Modeller, GCTF, MotionCorr2, clampfit, graphpad

For manuscripts utilizing custom algorithms or software that are central to the research but not yet described in published literature, software must be made available to editors/reviewers upon request. We strongly encourage code deposition in a community repository (e.g. GitHub). See the Nature Research guidelines for submitting code & software for further information.

Data

Policy information about availability of data

All manuscripts must include a data availability statement. This statement should provide the following information, where applicable:

- Accession codes, unique identifiers, or web links for publicly available datasets
- A list of figures that have associated raw data
- A description of any restrictions on data availability

The modeled atomic coordinates has been deposited in the Protein Data Bank with the accession code 5YD1 (AtOSCA1.1) and 5Z1F (AtOSCA3.1). In addition, EM maps have been deposited in EMDB with accession codes EMD-6822 (AtOSCA1.1) and EMD-6875 (AtOSCA3.1).

Field-specific reporting

Please select the best fit for your research. If you are not sure, read the appropriate sections before making your selection.

☒ Life sciences ☐ Behavioural & social sciences ☐ Ecological, evolutionary & environmental sciences

For a reference copy of the document with all sections, see nature.com/authors/policies/ReportingSummary-flat.pdf

Life sciences study design

All studies must disclose on these points even when the disclosure is negative.

Sample size	All of functional experiments were repeated at least 3 times and the sample size is determined based on the reproducibility of the experiments.
Data exclusions	Cryo-EM micrographs with ice were excluded manually. Particles belonging to bad classes were discarded and the data processing flowchart were summarized in Supplementary Figure 3 and 5.
Replication	All attempts at replication were successful
Randomization	For cryo-EM 3D refinement, all particles were randomly split into two groups.
Blinding	The investigators were blinded to group allocation during data collection and analysis.

Reporting for specific materials, systems and methods

Materials & experimental systems

n/a	Involved in the study
☒	☐ Unique biological materials
☒	☐ Antibodies
☐	☒ Eukaryotic cell lines
☒	☐ Palaeontology
☒	☐ Animals and other organisms
☒	☐ Human research participants

Methods

n/a	Involved in the study
☒	☐ ChIP-seq
☒	☐ Flow cytometry
☒	☐ MRI-based neuroimaging

Eukaryotic cell lines

Policy information about cell lines

Cell line source(s)	FreeStyle 293-F and sf9 are from Thermo Fisher Scientific.
Authentication	Cell line was directly purchased from Distributors. Cell line authentication was not performed
Mycoplasma contamination	FreeStyle 293-F and sf9 were negative for mycoplasma contamination.
Commonly misidentified lines (See ICLAC register)	N/A